Toward Prediction of Radiating Hypersonic Jet Exhaust Shock Waves

Fahad M. Nabid* and Steven A. E. Miller†
University of Florida, Gainesville, Florida, 32611

This study investigates hypersonic jet exhaust flow-fields at off-design conditions using Computational Fluid Dynamics (CFD) simulations and develops empirical models to capture the plume and internal shock waves' origin and angles. The analysis identifies internal, trailing, and plume shock waves in circular nozzles, showing how jet Mach number (M_j), static pressure ratio (SPR), static temperature ratio (STR), and freestream Mach number (M_∞) govern shock wave location, strength, and angular characteristics. Additionally, sensitivity analysis reveals that plume shock wave locations are primarily influenced by M_j and SPR, with higher values pushing shocks downstream and amplifying strength, while internal shock waves are strongly affected by density ratio and M_j, reflecting STR-driven jet dynamics. STR stabilizes downstream flow by promoting thermal diffusion, while higher SPR intensifies near-field compression waves. Empirical models predict plume shock wave origins with a root mean square error (RMSE) of 3.6%, internal shock wave origins with a RMSE of 4.4%, and shock wave angles with RMSE values of 3.65%, 3.65%, and 2.02% for internal, plume, and trailing shocks, respectively. These models accurately capture the nonlinear interactions between flow parameters, providing efficient tools to predict shock wave properties across off-design conditions with minimal computational expense.

Nomenclature

c	=	Speed of sound
D	=	Characteristic nozzle diameter
e_o	=	Total energy per unit mass
j	=	Jet exit properties
L	=	Length
M	=	Mach number
M_∞	=	Freestream Mach number
M_j	=	Jet exit Mach number
p	=	Pressure
p_∞	=	Freestream static pressure
p_r	=	Normalized pressure ratio
SPR	=	Static Pressure Ratio
Re	=	Reynolds number
r	=	Radius
rD^{-1}	=	Non-dimensional radial distance
STR	=	Static Temperature Ratio
T	=	Temperature
T_∞	=	Freestream static temperature
t	=	Time

*Ph.D. Student, National Defense Science and Engineering Graduate Fellow, Department of Mechanical and Aerospace Engineering, University of Florida, fahadnabid@ufl.edu, AIAA student member.

†DARPA Director's Fellow for Hypersonics and Associate Professor of Mechanical and Aerospace Engineering, Theoretical Fluid Dynamics and Turbulence Group, Department of Mechanical & Aerospace Engineering, University of Florida, 331 MAE-A, P. O. Box 116250, Gainesville, FL 32611, saem@ufl.edu; saemiller@gmail.com, AIAA Associate Fellow and lifetime member.

u, v, w = Cartesian velocity components
x, y, z = Cartesian spatial coordinates
xD^{-1} = Non-dimensional axial distance
α = Angle of attack
β_e = Plume shock angle
β_i = Internal shock angle
β_t = Trailing shock angle
ρ = Density
ρ_r = Normalized density ratio
∞ = Freestream properties

I. Introduction

The characteristics of sonic boom signatures produced by highly energetic turbulent wakes or jets from hypersonic movers are currently not well understood, but can be used for vehicle detection and characterization. These wakes or plumes from hypersonic movers and their signatures [1] extend for many miles. The sonic boom is created by the shock and expansion waves that radiate from the flight-vehicle and propagate long distances through the atmosphere [2]. Newly developed flight-vehicles, like the NASA X-59 [3], create low-boom waveforms that propagate through the atmosphere and may adversely affect communities and potentially cause annoyance. Traditional supersonic aircraft create sonic booms of greater intensity relative to low-boom flight-vehicles, which are often detected by ground observers as N-waves. Hypersonic sonic boom has unique properties [4] that must be considered. The detection, characterization, and mitigation of sonic booms are of great interest to the hypersonics defense community.

The propulsion of high-speed flight-vehicles creates an off-design jet exhaust flow-field due to the static pressure mismatch between the jet exhaust and the atmosphere. At supersonic conditions, instead of an internal shock cell structure, a new shock wave radiates from the exhaust, which must be predicted for sonic boom analysis. This represents an additional radiating shock wave that appears after the trailing edge or nozzle exit. It is not accounted for in traditional sonic boom theory, such as those predicted by the F-function, and not usually accounted for in Computational Fluid Dynamics (CFD) predictions of supersonic aircraft, nor integrated into sonic boom propagation codes for analysis.

For the purposes of design and sonic boom prediction for hypersonic, traditional supersonic, and low-boom waveform flight-vehicles, the dynamics of the exhaust shock wave, which radiates and is attached to the jet shear layer, are not well understood. This area of study requires further investigation to improve our comprehension and predictive capabilities. One experimental study conducted by NASA on supersonic exhaust shows that Nozzle Pressure Ratio (NPR) influences the behavior of trailing shock waves [5]. NPR is the ratio between the stagnation pressure, p_o, within the nozzle plenum and the ambient static pressure, p_∞. Generally, a higher NPR intensifies the exhaust shock wave, which interacts with the jet exhaust and modifies the sonic boom signature.

Figure 1 illustrates the shock wave structures within a jet plume, as detailed by Capone and Putnam [6]. A Prandtl–Meyer expansion at the plume exit generates internal shocks that propagate axially along the jet's centerline. These shocks interact with the surrounding shear layer, where the high-velocity jet flow meets the ambient fluid. The interaction causes a redistribution of pressure and momentum, leading to the formation of plume shock waves. These angled shocks radiate outward from the shear layer, shaping the exhaust plume.

Figure 2 provides complementary insight into jet plume behavior by visualizing the shock structure (Fig. 2a) and corresponding pressure measurements (Fig. 2b) along the near-field. Alternating compression and expansion waves within the plume form discrete shock cells. These cells are evident as bright and dark bands in schlieren imaging, aligning with the observations in Fig. 1.

The pressure profile in Fig. 2b further highlights key features of the plume dynamics. A sharp pressure rise at $xD^{-1} = 4$ (Fig. 2.b.ii.) marks the trailing shock wave. Similarly, the second pressure peak at $xD^{-1} = 6$ (Fig. 2.b.iii.) corresponds to the exhaust shock wave. These features demonstrate how the internal shocks, interacting with the flow boundary, contribute to the formation of large-scale plume shock waves, as shown in Fig. 1. Both figures highlight the coupled dynamics of internal shocks, boundary-layer interactions, and plume structures, crucial for understanding jet exhaust flow, predicting far-field noise, and analyzing plume heat transfer, as detailed in [6].

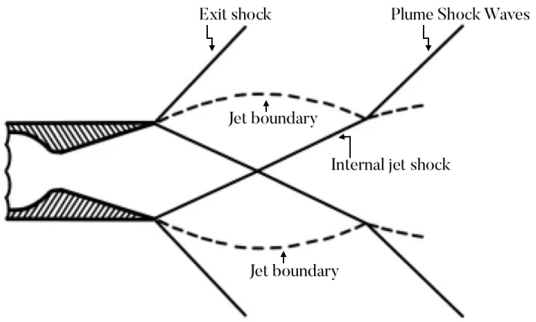

Fig. 1 Schematic representation of the jet exhaust shock pattern.

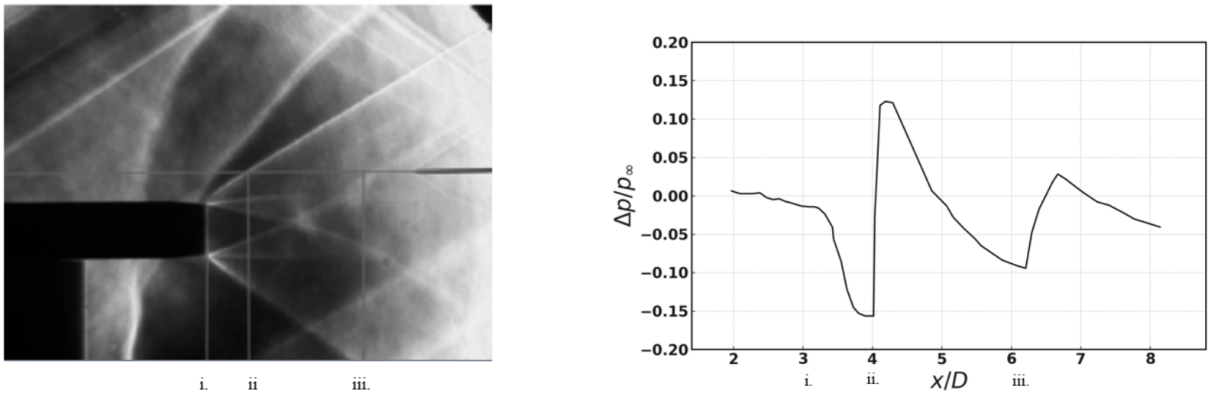

(a) Schlieren image

(b) Normalized static pressure

Fig. 2 Schlieren of an exhaust plume in a NASA Glenn Research Center (GRC) supersonic tunnel operating at NPR = 14. (a) Schlieren image and (b) normalized static pressure (see Castner [5]).

The CFD simulations of Castner et al. [7] show how the exhaust plume deflects shock waves and modifies the overall flow-field. These numerical predictions show significant changes (8 to 15 percent) in shock wave pressure amplitude due to the presence of the exhaust plume [7]. The study observed that exhaust the shock wave radiates from the jet and is attached to the jet shear layer. The typical internal shock cell structure is not present, and only very weak waves exist within the jet exhaust after the internal shock wave.

This paper presents the CFD predictions and analysis to study the flow-field dynamics of circular nozzles operating off-design at supersonic conditions. The purpose is to accurately predict the exhaust shock wave for sonic boom prediction, enhance the design of low boom flight-vehicles, understand the physics of the exhaust shock waves, and allow analysts to understand signals from hypersonic movers.

The physics of the flow-field is now described using traditional theory. See Fig. 3 in reference to the physical description. The origin of the coordinate system is at $\boldsymbol{x} = 0$, where the bold symbol represents a vector and $\boldsymbol{x}$ represents the spatial position relative to the center of the nozzle exit. Two parallel supersonic streams with distinct Mach numbers, M, and pressures, p, become a high-speed supersonic jet shear layer. The core stream, from the engine and representative of the jet exhaust, is characterized by subscripts denoting jet properties, subscripts j, (e.g. M_j, p_j, etc.) with a positive axial fully-expanded jet velocity, u_j. The ambient stream, denoted by subscript ∞, has properties M_∞, p_∞, a positive axial component u_∞, and a lateral component, $v_\infty \leq 0$. For simplicity, parallel streams can be examined by setting the velocity component $v_\infty = 0$. This latter value can either be zero, indicating parallel flow, or negative, reflecting the relative angle of the fuselage to the nozzle exit.

For circular nozzles and steady base flow-fields, the flow-field is axisymmetric about the centerline. On the centerline, the boundary condition is axisymmetric. At the nozzle lip line, $x = 0$ and $y = D/2$, these two streams converge to form a supersonic shear layer and represent the origin of the jet flow-field. A trailing shock wave, initiated at this location and characterized by subscript t, subsequently redirects the jet by a deflection angle θ_t, which is relative to the incoming

ambient flow-field. The trailing shock wave turning angle, θ_t, is relative to the initial ambient flow-field and exhaust, but for simplicity will be examined relative to the centerline. The core flow-field on the centerline is not turned due to the presence of the trailing shock wave. However, the core flow-field near the nozzle lip is also turned by the trailing shock wave.

The jet flow-field is off-design and a shock (or expansion system) develops initially from the nozzle exit. Figure 3 shows the expansion system at the nozzle exit, and implies that $p_j > p_\infty$. There are right and left-running characteristic waves or Mach waves within the flow-field. Left-running waves impinge on the jet shear layer and coalesce to a point downstream on the centerline of the axisymmetric flow-field. The origin of the internal shock wave is at x_i and $y_i = 0$. Also, right-running waves reflect from the centerline and subsequently alter the shear layer. This coalescence forms a new internal shock wave within the jet flow-field, with associated properties denoted by subscript i. This shock cell system is much like the traditional off-design jet in an ambient subsonic flow-field. However, the new left-running shock wave, when it impinges on the jet shear layer, is turned by a new angle and radiates as a new exhaust shock wave.

The exhaust shock wave is not attached to the body of the flight-vehicle, but radiates from the jet shear layer. This is denoted in Fig. 3 with subscript e. This shock wave contains a slightly different radiation angle than the internal and trailing shock wave. The angle and position of the exhaust shock wave are dictated by static pressure matching behind the exhaust shock wave and the internal shock wave. Furthermore, the flow-field behind the internal shock wave is nearly parallel to the centerline.

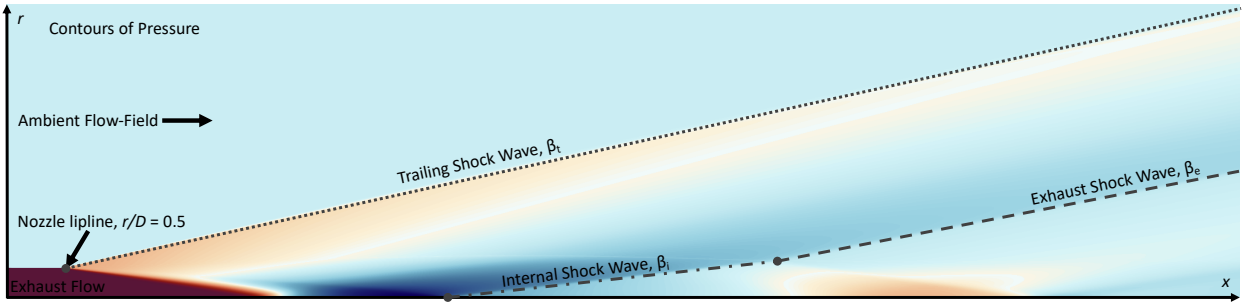

Fig. 3 Simplified physics of the formulation of the radiating exhaust shock wave from an off-design supersonic jet in an ambient supersonic flow-field.

For inviscid flow-fields, Landau's condition holds via interaction of p through the near-field aerodynamics if the leading or on-body shock and expansion waves are included. A relatively weak internal right-running wave is attached to the origin of the exhaust shock wave. Recall, the exhaust shock wave must be correctly predicted to accurately capture a sonic boom signature.

In this paper, the main focus is to capture the origin of the internal and plume shock waves via CFD simulations of a circular nozzle. This work is part of a broader effort aimed at developing an analytical solution for both circular and rectangular hypersonic nozzles, with a particular emphasis on locating plume and internal shock waves. Additionally, we present an empirical model to predict the origin locations and angles of the shock waves, along with detailed insights into the shock wave structures and their underlying physics. The results from this study will serve as valuable datasets for future analytical solutions. For this paper, the scope is limited to circular nozzles without considering variations in nozzle diameter.

In Section II, the methodology is outlined, covering the experimental setup, governing equations, and pre- and post-processing steps. Section III presents the results and a detailed discussion of the findings. Finally, Section IV concludes the paper, highlighting key findings, implications, and potential directions for future work.

II. Methodology

Numerical predictions of the flow-field are created using the NASA Fully Unstructured Navier-Stokes Three-Dimensional (FUN3D) CFD solver. The Euler equations, energy equation, and ideal gas law are used to generate a database of predictions to validate a new model which will be discussed in this paper later on. A large database of predictions using adjoint-based mesh adaptation is being produced for this purpose. Overpressure, shock wave statistics, and positions are extracted automatically using FUN3D post-processing tools such as Python scripts and Tecplot. This section will discuss the development of the simulation, the governing equation, and pre- and post-processing methods.

A. FUN3D

The NASA FUN3D solver is used to create predictions of the flow-field. FUN3D is a finite-volume solver [8–11]. FUN3D stores flow-variables at the vertices or nodes of the computational grid. The inviscid fluxes at interfaces between neighboring control volumes are calculated using an approximate Riemann solver, which utilizes the values from both sides of the interface [12]. FUN3D offers several options for convective flux schemes [13]. The FUN3D solver has an adjoint-based mesh adaptation scheme, which is used in the present approach. This allows for the shock waves to be captured through an adapted optimized computational grid. The adjoint mesh adaptation approach provides the sensitivity of the near-field pressure signature [14], which depends on a cost function.

B. Governing Equations

Though the physics of hypersonic flows requires the use of the full Navier-Stokes equations with appropriate gas laws, chemistry, radiation, and electromagnetics, the Euler equations are selected for the present study. This is due to the programmatic goal of creating a separate analytical model that will be systematically validated with a large numerical database. These other effects will be integrated later in the program.

For the circular nozzles, the Euler equations are solved in their Cartesian form, even though the flow-field from a circular nozzle is axisymmetric. The Euler equations are closed by the energy equation with field-variable static pressure, p. The ideal gas law is used for the calculations.

C. Domain and Boundary Conditions

A three-dimensional computational domain is created that includes the nozzle, exhaust plume, and ambient domain. The CFD domain is one-fourth of the cylindrical domain. The length of the domain in the streamwise direction is $70D$, where D is the nozzle exit diameter, and the cross-stream direction extends from the nozzle centerline to $15D$, as shown in Fig. 4. This domain is large enough to capture shock waves for the present off-design condition used in the simulations.

The length of the nozzle from inlet to exit is one D, see Fig. 4. The nozzle lipline has been placed at $rD^{-1} = 1/2$, and a slip boundary condition is applied. Note that the nozzle contour and exterior geometry are not included in the present study so as not to alter the dynamics of the exhaust and ease the creation of an analytical model. It is best practice to include the nozzle geometry in the calculation as it alters the exhaust profile at the nozzle exit. For the purpose of model development, a single baffle is used to isolate this effect.

A three-dimensional quarter-section of the cylindrical domain is simulated using FUN3D. The boundary conditions are illustrated in Fig. 4. The top boundary is set to a far-field conditions which is Riemann invariant. This reduces the reflection of outgoing radiating shock waves. An ambient inflow boundary condition (upper left) above the nozzle lipline is set to a freestream boundary condition. On the right side of the domain, a supersonic extrapolation boundary condition is applied to allow the flow to exit without reflection.

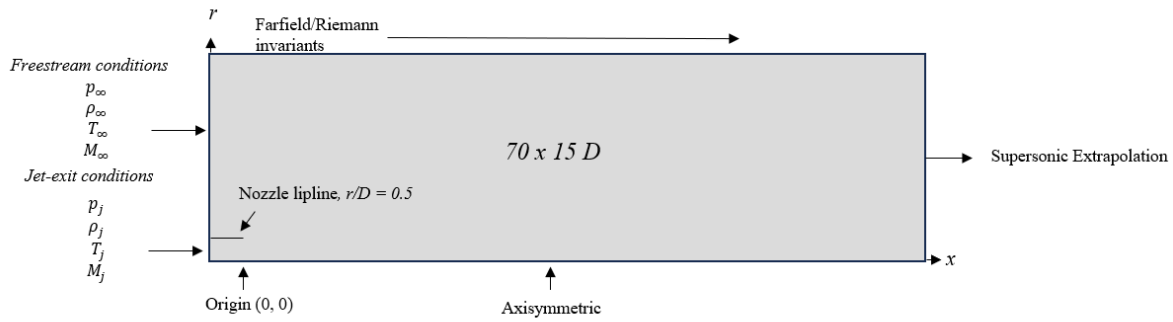

Fig. 4 Computational domain and boundary conditions for the FUN3D simulation.

The jet-exit which can be seen bottom left corner is set to a supersonic inlet. Two symmetric boundary conditions are placed in planes of symmetry. These are located in the $x - y$ and $x - z$ planes of the flow-field, which correspond to the coordinate system. The x-axis is specified as an axisymmetric condition.

We use a near-field pressure cost function, which evaluates the accuracy of near-field pressure signatures by summing the squared differences between the local static pressure and ambient static pressure along rays aligned with the freestream direction. Adjoint-based grid adaptation produces anisotropic mesh elements, particularly near shock waves, refining the mesh to capture anisotropic flow features such as shock waves and boundary layers more effectively [15–17].

Adjoint-based mesh adaptation is performed using p and ρ gradients at 12 locations of $rD^{-1} = 0.0001, 0.2$, 0.3, 0.4, 0.53, 1, 1.5, 2, 2.5, 3, 4, and 5. The anisotropy value is set to 1×10^3 and the complexity value to 1×10^6 to manage mesh complexity and maintain computational efficiency. The anisotropy value limits the ratio of the largest to the smallest spacing in the mesh, ensuring that the grid can adapt to highly anisotropic features in the flow without becoming excessively distorted. A higher anisotropy value allows the mesh to stretch more in one direction, which is particularly useful for capturing boundary layers and shock waves accurately. The complexity value controls the mesh's total number of elements, directly affecting the resolution and computational cost. Figure 5a shows the initial coarse mesh with approximately 22.14 thousand cells, while Fig. 5b shows the optimized mesh with approximately 16 million cells. The optimized mesh features fine, stretched cells along the surfaces of the shock waves (see Fig. 5b).

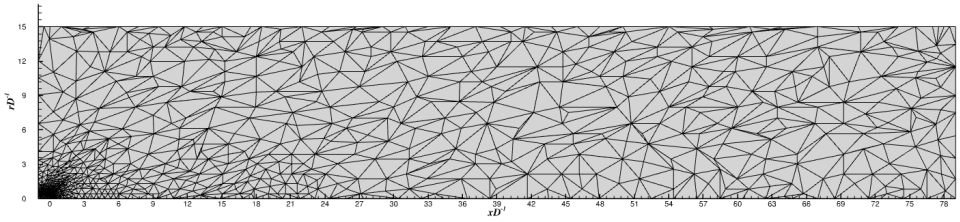

(a) Initial Mesh

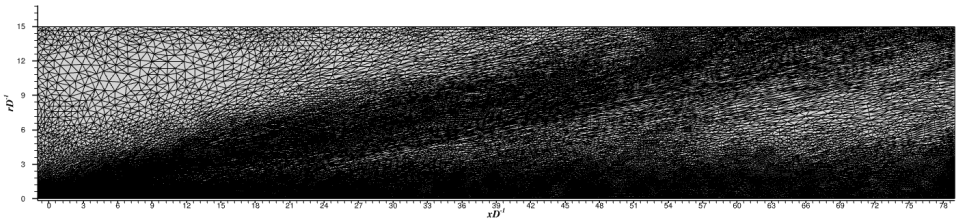

(b) Optimized Mesh

Fig. 5 Comparison of Mesh Adaptation: (a) Initial Mesh before refinement and (b) Optimized Mesh after adaptation.

D. Computational Approach

The Harten-Lax-van Leer with Einfeldt extension with improved (HLLE++) scheme is used for these simulations. This improved shock-capturing method is designed for high-speed flows on non-shock-aligned grids. It reduces the reliance on eigenvalue limiting, which is required in Roe's scheme, by switching to a more dissipative algorithm near strong shock waves. A shock sensor detects the presence of shock waves, and the method dynamically adjusts dissipation to stabilize the solution. This approach blends between modified Modified Harten-Lax-van Leer with Einfeldt (HLLE+) and Roe eigenvalues to capture shock waves robustly, requiring minimal tuning. The HLLE++ scheme improves predictions for high-speed shear layer interactions with shock waves due to its low numerical dissipation, effective shock-capturing capabilities, and enhanced numerical stability [18, 19]. It performs particularly well in hypersonic flows, offering increased accuracy and robustness compared to traditional methods [20].

We use the Monotone Upstream-Centered Schemes for Conservation Laws (MUSCL) reconstruction scheme for unstructured grids, UMUSCL. This scheme separates spatial and temporal accuracy, allowing for enhanced accuracy of the numerical solution. The U-MUSCL parameter, κ controls the interpolation of variables at cell faces. This ensures that the scheme remains monotone and reduces spurious oscillations near shock waves. For the present predictions, $\kappa -$ UMUSCL = 0.5, which provides third-order accuracy while balancing numerical stability with enhanced shock wave resolution [21].

The H-van Albada (heuristic van Albada) flux limiter is a stencil-based limiter augmented with a heuristic pressure

limiter, which relies on a single coefficient to fine-tune its behavior, balancing numerical dissipation and stability [13]. It is chosen for its effectiveness in preventing spurious numerical oscillations near discontinuities while maintaining high resolution in capturing shock waves and other flow features [22]. This flux limiter is particularly suitable for simulations involving hypersonic flows, where accurate shock wave resolution is required [23]. The limiter works by blending high-order and low-order discretizations based on the local flow conditions, ensuring that the scheme remains monotone and reduces spurious oscillations near shock waves.

Implicit time integration is employed to predict statistically stationary (steady) solutions. This approach is particularly advantageous for high-speed flow simulations, as it enables the use of larger time steps without compromising accuracy or stability. Furthermore, this method facilitates the simulation in reaching a steady-state solution. The Generalized Conjugate Residual (GCR) method is used to stabilize and accelerate convergence [13]. Mean flow-field sweeps are set to two. It is important to note that, the mesh adaptation scheme has to run for both low Mach numbers and high Mach numbers separately because shock waves angle, β, decrease with increasing M. The mesh adaptation is performed separately for supersonic and hypersonic freestream conditions because the trailing shock angles in hypersonic cases are smaller than those in supersonic cases. This separate adaptation enhances the sharpness of shocks during the simulation, reduces the required number of grid points, saves simulation time, and ensures that grid stretching aligns correctly with the direction of shock waves.

E. Post-Processing

The post-processing for this study utilizes Tecplot and custom Python scripts. The `fun3d.nml` file is configured at the beginning of the simulation to specify output settings, such as the volume of the computational domain, the pressure distribution at specified r/D values, and the residuals, which are written during the simulation as it progresses. During the simulation, both input and output variables are kept dimensionless. However, for contour visualization, the data is dimensionalized using air properties at an altitude of 50,000 feet, where the density ρ is 0.1951 kg/m^3, the pressure p is 12.13 kPa, the temperature T is 217 K, and the speed of sound c is 295.07 m/s.

In this section, we detail the post-simulation techniques. The volume domain file generated from FUN3D is first loaded into Tecplot, where a slice is taken along the centerline in the $x - y$ plane, providing a 2D representation of the flow-field. This 2D slice is visualized in Tecplot to generate flow contours and further analyze key flow parameters such as pressure, density, temperature, Mach number, and the pressure ratio, $\Delta p/p_\infty$. Additionally, a numerical schlieren contour of the density gradient $\frac{d\rho}{dy}$ is generated to visualize the shock wave structure.

The pressure signature is directly extracted from the simulation using the sonic boom name-list from FUN3D. Subsequently, the data is processed using both Tecplot and a Python script. The Python script also analyzes the residual data. The shock wave angle is calculated based on the pressure signature using the following approach. The Python script reads the pressure signature data from a `.dat` file and identifies local maxima and minima in the pressure signals for multiple measurement points. The shock wave locations are determined by analyzing the pressure drop and the subsequent rise across the measurement points. For each signal, the script calculates the shock wave location as the point midway between the absolute minimum in pressure and the first local peak. The shock wave angles are computed between pairs of signals using

$$\theta = \arctan\left(\frac{\Delta y}{\Delta x}\right), \tag{1}$$

where Δy is the difference in the level (pressure ratio) between the two signals, and Δx is the difference in shock wave locations. Additionally, the script calculates the trailing shock wave locations for specific signals using the initial rise method, which identifies the first local maximum after a near-zero value in the pressure signal. From these locations, the trailing shock wave angles are similarly calculated and recorded. All results, including shock wave locations, shock wave angles, trailing shock wave locations, and trailing shock wave angles, are written to a text file and a `.csv` file for further analysis.

The shock wave origin is manually determined using density contours due to the presence of curved shock waves near the mixing layer. Initially, a linear extrapolation is attempted to estimate the shock wave origin; however, it is not viable due to the extreme shock wave curve because of expansion waves within the mixing layer and near-field. After gathering the shock wave origin data, it is analyzed with Python and compared against the off-design variables.

In this study, static pressure ratio (SPR) and static temperature ratio (STR) are used to characterize the flow conditions instead of NPR and Total Temperature Ratios (TTR). The analysis does not include nozzle diameter and varies M_j for the simulations.

SPR, defined as the ratio of static pressures p_j/p_∞, and STR, defined as the ratio of static temperatures T_j/T_∞, provide a localized measure of flow properties directly relevant to static flow conditions. In contrast, NPR and TTR are nozzle pressure or temperature ratios compared to the ambient pressure or temperature ratio, which are dependent on the M_j and the nozzle diameter. This choice simplifies the analysis, focusing on the physics of shock wave origins and angles without introducing geometric or Mach number dependencies, making SPR and STR more suitable for the development of the empirical models presented.

The boundary conditions for the current set of High-Performance Computing (HPC) simulations are presented in Table 1. This table summarizes the key parameters of the boundary conditions, including M_∞, M_j, SPR, and STR. These parameters were carefully selected to ensure that the simulations operate in an off-design regime. Furthermore, the condition $M_\infty < M_j$ is strictly maintained, ensuring that the jet Mach number exceeds the freestream Mach number to represent realistic jet flow interactions. The ambient conditions are set to correspond to an altitude of 50,000 feet, representing high-altitude, low-pressure atmospheric conditions for the simulations.

Table 1 Simulated Boundary Conditions.

Parameter	**Values**
M_∞	1.2, 1.414, 1.6, 2.2, 3.2, 5, 6, 7, 8, 9, 10
M_j	1.86, 3.40, 5.00, 6.00, 7.00, 8.00, 9.00, 10.00, 11.00, 12.00
SPR	1.97, 2.10, 3.50, 7.00
STR	1.38, 4.61, 5.76, 6.91

The dynamic static pressure ratio p_r and density ratio ρ_r are dimensionless parameters used to characterize flow conditions in terms of pressure and density. The dynamic static pressure ratio p_r is defined as $p_r = p_j/(c_\infty^2 \rho_\infty)$, where p_j is the jet static pressure, c_∞ is the speed of sound in the freestream, and ρ_∞ is the freestream density. Similarly, the density ratio ρ_r represents the ratio of jet density to freestream density and is calculated as $\rho_r = \rho_j/\rho_\infty$, where ρ_j is the jet density and ρ_∞ is the freestream density. These parameters provide normalized measures of pressure and density variations relative to the freestream conditions, making them crucial for analyzing and comparing different flow regimes. Table 2 shows conversions for SPR, STR, p_r, and ρ_r.

Table 2 SPR, STR, p_r, ρ_r conversions.

SPR	**STR**	p_r	ρ_r
2.10	4.60	1.5	0.46
3.50	4.60	2.5	0.76
7.00	4.60	5.0	1.52
2.10	5.76	1.5	0.36
3.50	5.76	2.5	0.61
7.00	5.76	5.0	1.21
2.10	6.91	1.5	0.30
3.50	6.91	2.5	0.51
7.00	6.91	5.0	1.01
1.97	1.38	1.41	1.43

In this paper, p_r and ρ_r are used as empirical models, representing normalized pressure and density ratios for FUN3D inputs. The pressure ratio p_r is derived from the dynamic pressure of the ambient environment, while the density ratio ρ_r is driven by the ambient density ratio. These normalized parameters are critical for describing the boundary conditions in the simulation framework.

III. Results and Discussions

The simulated results from Table 1 are presented in this section. All the cases have been simulated using the University of Florida's HiPerGator HPC cluster. All simulations are converged and represent the solution of the steady discretized flow-fields.

A. FUN3D Simulations, Flow-fields and Shock Wave Structures

All cases are run until residual convergence is achieved, ensuring the stability and accuracy of the numerical solution. Residual convergence is monitored across key flow variables, including density ρ, momentum components u, v, w, and energy p_e, as shown in Fig. 6. The residuals are reduced by at least three orders of magnitude. For low Mach number cases, where $M_\infty < 9$, the simulation typically requires twelve to eighteen thousand iterations to achieve convergence. However, for $9 \leq M_\infty \leq 10$, the simulations require over twenty-four thousand iterations to converge.

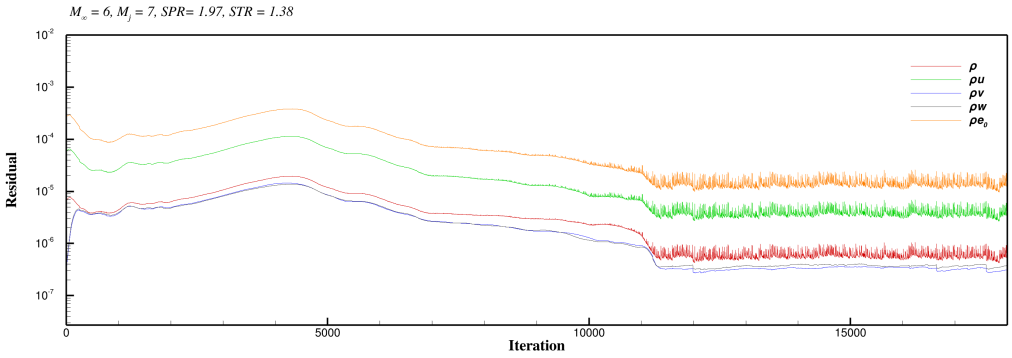

Fig. 6 Residual plot for $M_\infty = 6$, $M_j = 7$, SPR = 1.97, and STR = 1.38.

Figure 7 shows the p contours for $M_j = 7.00$, $M_\infty = 6.00$, $SPR = 1.97$, and $STR = 1.38$. Near the nozzle exit, the flow expands rapidly due to a pressure mismatch, forming internal shock waves within the jet. The blue region represents the low-pressure jet plume, while the oblique internal shock waves and expansion waves govern the pressure oscillations along the jet axis. These internal shock waves interact with the high-speed shear layer, forming plume shock waves. It is visible from Fig. 7 that the internal and plume shock waves have different angles due to the shear layer. The pressure gradients reflect the periodic compression and expansion zones typical of under-expanded supersonic jets. These features illustrate the flow's adjustment to ambient conditions downstream.

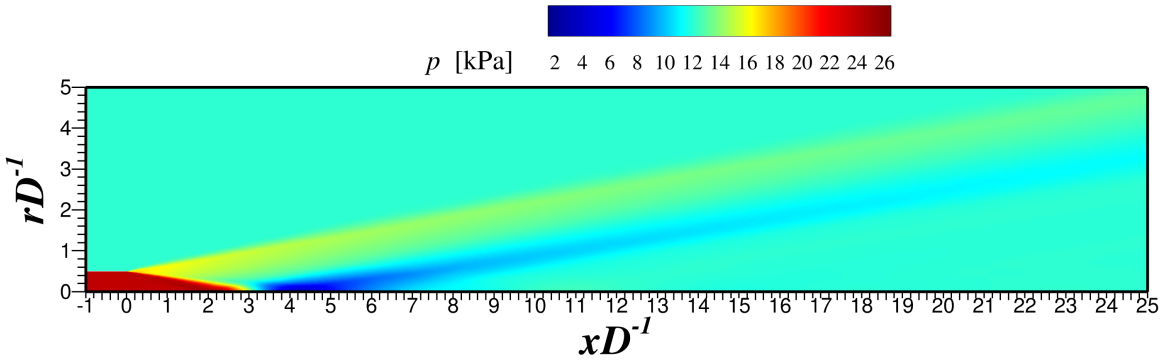

Fig. 7 Contours of p at $M_\infty = 6.00$, $M_j = 7.00$, SPR = 1.97, and STR = 1.38.

In Fig. 8, the ρ contour shows a jet exhaust with trailing shock wave, internal shock wave, and plume shock wave. The high-density core near the origin represents the exhaust flow with trailing shock wave propagating downstream. An internal shock wave forms within the core while the plume shock wave attaches to the shear layer. The density gradient reveals the presence of shock wave structures illustrating their impact on redirecting and compressing the flow,

contributing to the jet's dispersion and energy dissipation into the ambient. This contour plot shows the internal shock wave as the blue region within the shear layer near the centerline. The internal shock wave radiates outward and interacts with the shear layer, identifiable as the green region in the density contour plot. This interaction generates another shock wave downstream, the plume shock wave, which normalizes the expansion waves originating from the trailing shock wave.

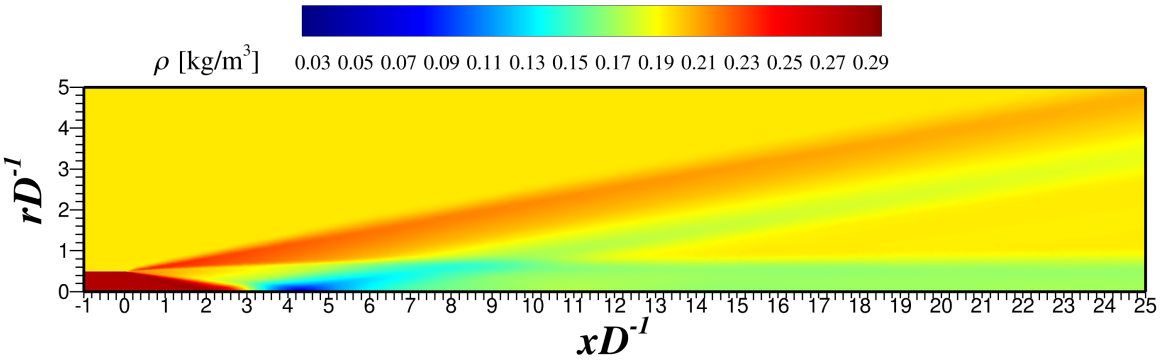

Fig. 8 Contours of ρ at M_∞ = 6.00, M_j = 7.00, SPR = 1.97, and STR = 1.38.

Figure 9 shows the static temperature T distribution in a jet flow. The temperature ranges from 140 K (dark blue) to 300 K (red), illustrating significant thermal variations across the domain. A high-temperature core near the jet axis close to the origin appears in red and orange hues, representing heated exhaust gases exiting the nozzle at high velocity. As the flow progresses, the temperature rises due to shock waves but reduces during jet expansion. Downstream, the plume shock wave following the trailing shock wave increases the temperature again, approaching ambient levels. A low-temperature region in the shear layer appears as green and blue hues, caused by internal shock waves lowering the temperature locally. The temperature decreases as the jet mixes with ambient air and drops sharply radially away from the jet axis, confining the high-temperature core.

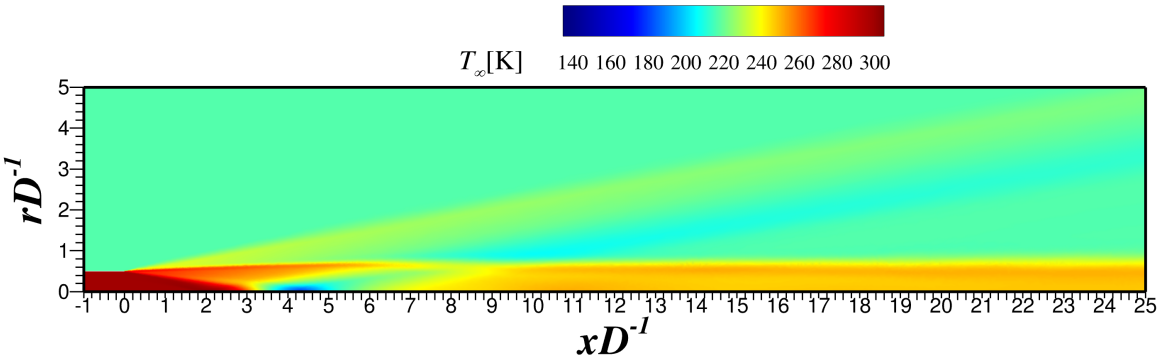

Fig. 9 Contours of ρ at M_∞ = 6.00, M_j = 7.00, SPR = 1.97, and STR = 1.38.

The schlieren contour plot with density gradients ($\partial\rho/\partial y$) is shown in Fig. 10, highlighting shocks and flow interactions. Dark and light bands indicate steep density changes caused by shock waves and shear layer dynamics. Near the nozzle, sharp gradients along the centerline correspond to internal shock waves in the jet core resulting from compressible flow effects. These shock waves interact with the shear layer, where the jet mixes with ambient air, forming outward-radiating gradients. The plume shock wave appears downstream, signifying re-compression after the trailing shock wave's expansion. As shown, Fig. 10 captures the structure of shock waves, expansion waves, and shear layers.

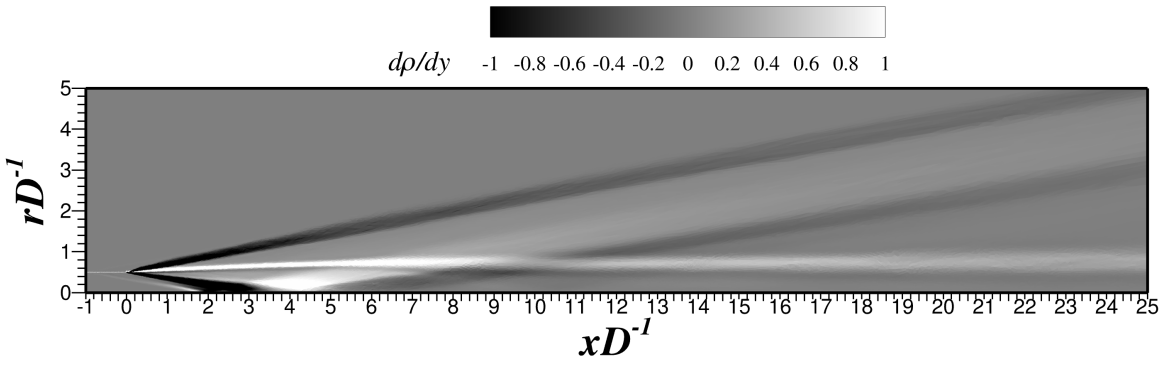

Fig. 10 Schlieren contours illustrating flow physics at $M_\infty = 6.00$, $M_j = 7.00$, SPR = 1.97, and STR = 1.38.

B. Benchmark Comparison: SU2 vs. FUN3D Line-Plot Analysis

The simulated near-field results have been benchmarked against data obtained from the SU2 simulation, an open-source multiphysics simulation and design software. Both simulations were conducted under identical flow conditions, with a M_∞ of 5, M_j of 7, SPR of 1.97, and STR of 1.38. For the SU2 simulation, a 2D axisymmetric condition was assumed, utilizing the Advection Upstream Splitting Method (AUSM) flux limiter to ensure accuracy and numerical stability.

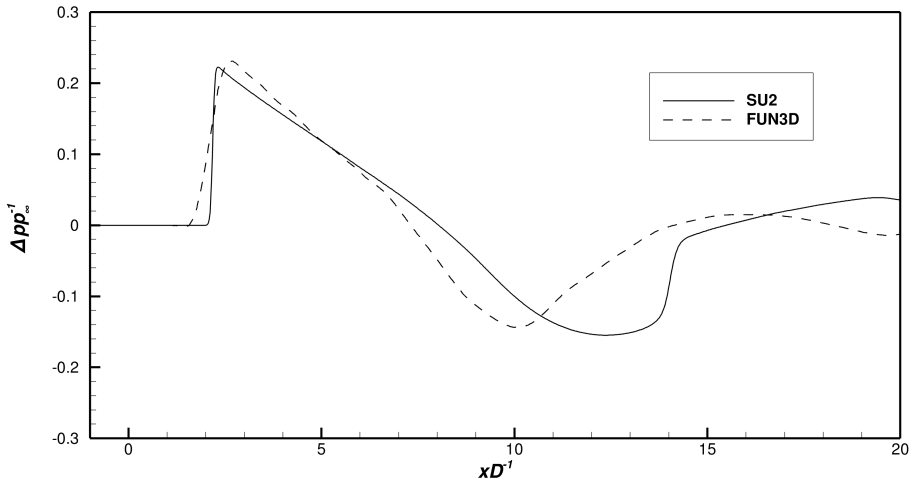

Fig. 11 Comparison of overpressure predictions at $rD^{-1} = 1$ for $M_\infty = 5$, $M_j = 7$, SPR = 1.97, and STR = 1.38 from SU2 and FUN3D simulations.

Figure 11 compares the near-field overpressure ($\Delta p/p_\infty$) at $rD^{-1} = 1$ along the normalized streamwise distance (xD^{-1}) for SU2 and FUN3D simulations under identical conditions. SU2 predicts sharper pressure gradients near the initial peak ($xD^{-1} < 5$), with a shock thickness that is consistent with expectations for high-speed flows, where shock thickness is typically very small. In contrast, FUN3D, employing the HLLE++ flux in 3D, produces smoother profiles downstream, particularly in the oscillatory regions ($xD^{-1} > 5$), which is attributed to HLLE++ flux's capability to enhance numerical stability. While the AUSM flux in SU2 captures sharper shock waves, FUN3D results exhibit broader shock regions. Despite these differences, both simulations predict similar overpressure profiles and shock angles, as seen in Figure 11.

C. M_j Effect on the Near-field Pressure Signature

In Fig.12a, as M_j increases, the initial overpressure peak becomes sharper, indicating stronger jet expansion and shock wave formation due to the higher jet exit velocity. The second rise in pressure corresponds to the plume shock wave, which moves further downstream and becomes less distinct as M_j increases. This shift occurs because the higher momentum of the jet delays the plume shock wave formation and dissipates its intensity more effectively. Beyond $xD^{-1} = 10$, the oscillations in pressure diminish with increasing M_j, showing that the flow stabilizes more quickly at higher jet Mach numbers. The results suggest that increasing M_j amplifies the initial shock wave's strength but reduces the plume shock wave's prominence and accelerates the transition to a steady downstream flow.

D. SPR Effect on the Near-field Pressure Signature

In Fig. 12b, as SPR increases, the initial overpressure peak rises significantly, highlighting the stronger shock waves generated by higher NPR. Since SPR and NPR are highly correlated, SPR is used in this analysis to characterize the flow behavior in the absence of an actual nozzle exit diameter. This substitution provides a reliable proxy for analyzing shock wave strength and flow properties under different operating conditions.

The elevated SPR values lead to stronger compression waves, consistent with shock wave theory, where increased upstream stagnation pressure amplifies shock wave strength and steepens pressure gradients in the near-field region ($xD^{-1} < 5$). The second pressure rise, associated with the plume shock wave, intensifies and shifts downstream as SPR increases. This behavior reflects a delayed stabilization of the plume, driven by the higher energy in the flow and the interaction between shock wave propagation and thermodynamic jet expansion. Higher SPR reduces the ratio of post-shock to pre-shock pressures, causing a more gradual adjustment of the flow.

In the far-field region ($xD^{-1} > 10$), the pressure signatures converge irrespective of SPR, underscoring the dissipative nature of high-speed flows. In higher speed regimes, viscous and thermal diffusion play a dominant role in mitigating the disparities introduced by varying SPR, leading to flow equilibration downstream. This behavior demonstrates that higher SPR primarily affects near-field dynamics by influencing shock wave strength and position, while the far-field behavior is governed by dissipation and stabilization processes. The use of SPR in this study ensures an accurate representation of flow properties in the absence of direct nozzle geometry specifications.

E. STR Effect on the Near-field Pressure Signature

Figure 12c illustrates that increasing STR leaves the initial overpressure peak largely unaffected, indicating that the incident shock wave strength is primarily governed by the upstream conditions and remains independent of downstream thermal effects. Beyond $xD^{-1} = 5$, higher STR significantly reduces the oscillation amplitudes, reflecting a stabilization mechanism driven by enhanced thermal diffusion and energy redistribution. The plume shock wave weakens, and its downstream pressure fluctuations dampen as STR increases, consistent with the thermodynamic principle that higher thermal energy promotes flow equilibration. This behavior aligns with shock wave theory, where elevated downstream temperatures lower the Mach number relative to local sound speed, diminishing the relative strength of secondary shock wave interactions. In high-speed flows, these effects highlight the role of STR in mitigating unsteady flow structures, leading to a more uniform pressure distribution in the far-field. Overall, STR primarily influences the dissipation and stabilization of post-shock wave flow structures, while the initial shock wave dynamics remain dictated by upstream flow properties.

F. Empirical Model for the Plume and Internal Shock Waves Origin

Empirical equations are developed based on the numerical database. These empirical models result from analyzing data collected from FUN3D simulations under various conditions but are validated only for the hypersonic region to focus on the paper objective, which is defined as $M_\infty = 5$ to 10, $M_j = 6$ to 12, $p_r = 1.2$ to 5, and $\rho_r = 0.1$ to 1.5. The models incorporate power and interaction terms to capture nonlinear relationships in the data. Parameters undergo optimization using nonlinear least squares fitting, and the models refine iteratively to ensure accuracy. Validation compares the model predictions with simulation data across the specified range of conditions, confirming the models' validity within this region.

The exhaust shock wave origin streamwise location is predicted with,

$$\begin{aligned}\left(\frac{x}{D}\right)_e \approx\ & 0.0288 M_\infty^{1.0806} M_j^{1.6684} p_r^{0.6289} \rho_r^{0.2458} - 0.1636 M_j^2 + 0.2586 p_r^2 - 1.0376 M_j p_r + 3.9592 p_r \\ & + 3.2182 \rho_r + 3.8954 M_j - 1.9415 M_\infty - 3.6583.\end{aligned} \tag{2}$$

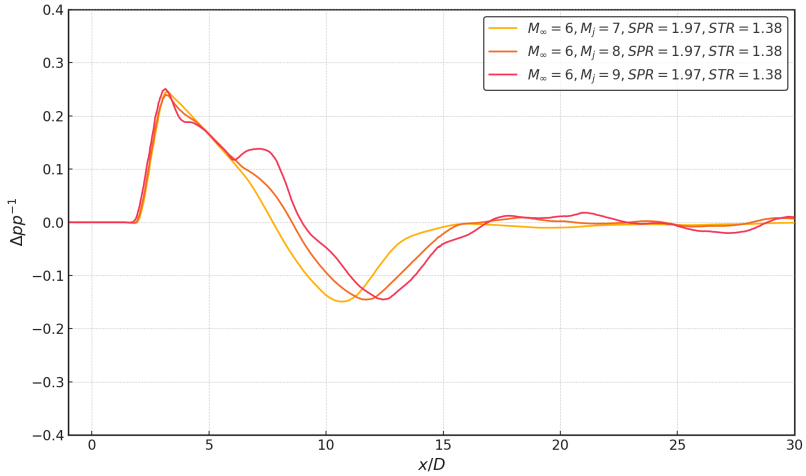

(a) Mach Sweep

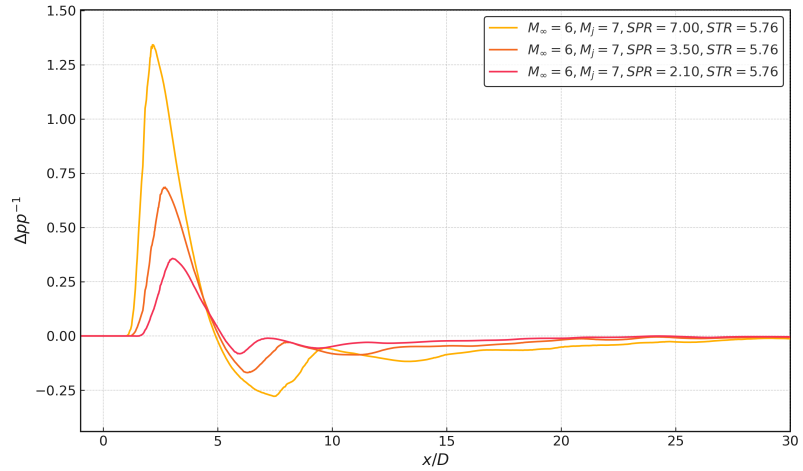

(b) Pressure Sweep

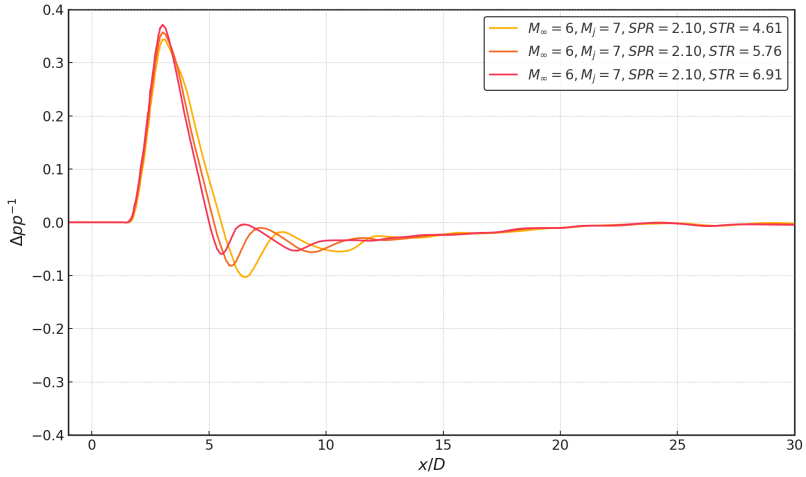

(c) Temperature Sweep

Fig. 12 Near-field pressure signature for $rD^{-1} = 1$. Each plot illustrates the influence of different parameters: (a) Mach sweep, (b) pressure sweep, and (c) temperature sweep.

The empirical model demonstrates close agreement with the FUN3D simulation data in predicting the plume shock wave origin location (xD^{-1}) across the range of conditions it is validated for, which are $M_\infty = 5$ to 10, $M_j = 6$ to 12, $p_r = 1.2$ to 5, and $\rho_r = 0.1$ to 1.5. As shown in Fig. 13, Eqn. 2 example validation is presented for $M_\infty = 7$, $p_r = 1.5$, $\rho_r = 0.3$, and $M_j = 8$ to 12. The root mean square error (RMSE) is calculated as 0.32, corresponding to approximately 3.6% of the average FUN3D simulated values. Both the empirical model and simulation data exhibit a similar nonlinear trend, with the plume shock wave location increasing as M_j rises. The largest deviations occur at the higher end of the range ($M_j = 11, 12$), where the empirical model slightly under-predicts the location compared to data from FUN3D.

The model's structure, which includes power-law and interaction terms, enables it to effectively capture the nonlinear relationships between the parameters ($M_\infty, M_j, p_r, \rho_r$) and the plume shock wave location. A sensitivity analysis of the empirical model reveals that the plume shock wave origin location (xD^{-1}) is most influenced by variations in M_j, followed by p_r, ρ_r, and M_∞. The high power-law exponent for M_j (1.6684) highlights its dominant role in determining the shock wave location, with small changes in M_j resulting in significant shifts in xD^{-1}. The parameters p_r and ρ_r exhibit moderate sensitivities, primarily affecting the plume shock wave location through their respective interaction and power terms. The influence of M_∞ is less crucial, acting as a scaling factor with a lower power-law exponent.

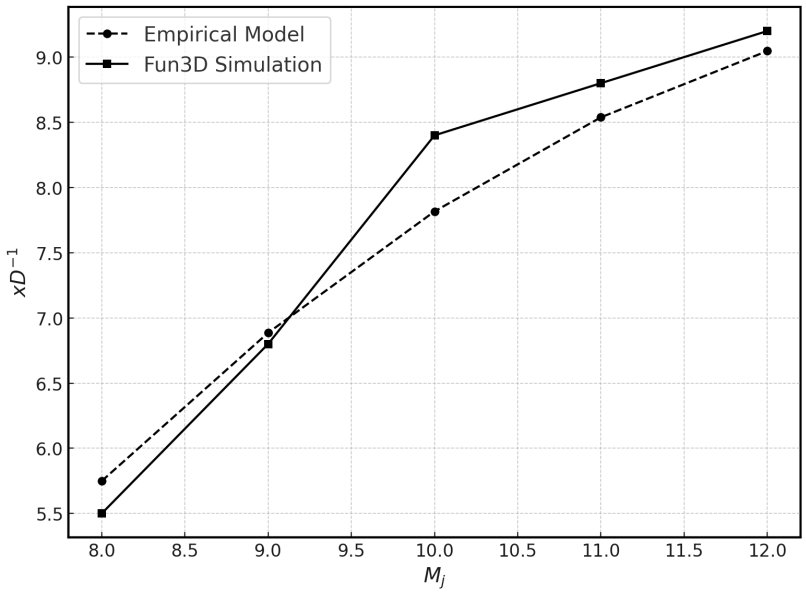

Fig. 13 Plume shock waves origin location vs M_j of $M_\infty = 7$, SPR = 2.1 and STR = 6.91.

The wave origin of the internal shock wave is

$$\left(\frac{x}{D}\right)_i \approx 44.8867 M_\infty^{0.0432} M_j^{0.9988} p_r^{0.0032} \rho_r^{0.9901} + 0.0324 M_j^2 - 0.1573 p_r^2 + 0.1321 \rho_r^2 - 0.0009 M_j p_r - 48.2460 M_j \rho_r - 0.0784 p_r \rho_r - 0.0010 M_j^3 + 0.0158 p_r^3 - 1.4618 M_\infty + 9.0561. \quad (3)$$

The empirical equation (Eqn. 3) demonstrates strong capability in predicting the origin of the internal shock wave (xD^{-1}), achieving an RMSE of 0.16, which corresponds to 4.4% of the average FUN3D simulation values. As shown in Fig. 14, the empirical model closely captures the nonlinear increase in shock wave origin location with increasing M_j. The plot highlights a good agreement across the range of $M_j = 8$ to 12, with the model effectively tracking the simulation trend, especially in capturing the steep rise in xD^{-1} between $M_j = 9$ and $M_j = 11$. This alignment validates the model's ability to account for the underlying jet dynamics and parameter interactions governing internal shock wave formation.

Sensitivity analysis of the equation reveals that M_j is the dominant parameter, with a near-linear primary term ($M_j^{0.9988}$) and significant higher-order terms (M_j^2, M_j^3) and cross-interactions ($M_j \rho_r$). These terms effectively account for the role of increasing jet velocity in strengthening the shock wave and pushing its origin downstream. The high sensitivity to M_j reflects the well-known relationship between jet velocity and shock wave formation in compressible flows. ρ_r is the second most significant parameter, with a strong exponent (0.9901) and interactions ($M_j \rho_r$, $p_r \rho_r$),

highlighting its influence on the density-driven dynamics that affect shock wave propagation. p_r has moderate sensitivity, contributing nonlinear effects through terms like p_r^2, p_r^3, and interactions with M_j and ρ_r. These terms capture the impact of pressure ratios on flow compression and expansion, which modulate the shock wave's location. In contrast, M_∞ has a negligible effect on the model's output, with a small exponent (0.0432), reflecting the limited influence of freestream conditions compared to jet-dominated dynamics in determining internal shock wave behavior.

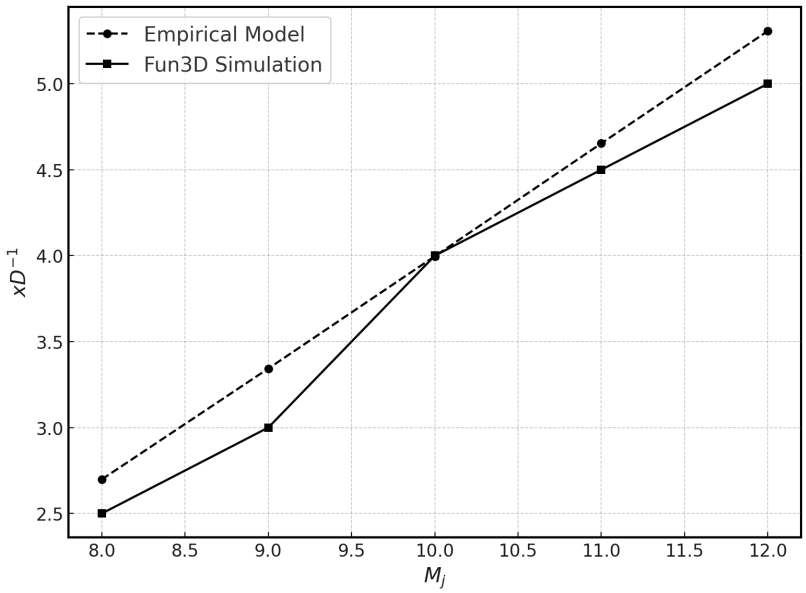

Fig. 14 Internal shock waves origin location versus M_j of $M_\infty = 7$, SPR = 2.1, and STR = 6.91.

G. Empirical Model for the Plume and Internal Shock Wave Angles

The data gathered from the FUN3D simulations provide detailed pressure signatures across various conditions. These pressure signatures are processed to calculate the angles of shock waves using the equations outlined in Eqn. 1. The correlations between the flow parameters and the behavior of the shock waves are identified by analyzing the calculated shock wave angles. This analysis enables the development of an empirical model that accurately predicts the shock wave angles.

This section presents an empirical model for the internal shock wave angle β_i, plume shock wave angle β_e, and trailing shock wave angle β_t. The model, based on M_∞, M_j, p_r, and ρ_r, accounts for nonlinear interactions in shock wave dynamics. Coefficients are derived using nonlinear regression on simulation data, ensuring the model effectively represents shock wave behavior. It provides a practical tool for predicting shock wave angles in similar flow regimes and aligns with the region defined for the shock wave origin empirical model.
The wave angle of the internal shock wave is

$$\begin{aligned}\beta_i \approx\, & 38.94 - 1.027M - 4.628M_j - 0.753p_r + 2.372\rho_r + 0.187M^2 - 0.159MM_j + 0.116Mp_r - 1.320M\rho_r \\ & + 0.201M_j^2 + 0.347M_jp_r + 0.317M_j\rho_r - 0.495p_r^2 + 0.024p_r\rho_r + 2.383\rho_r^2,\end{aligned} \tag{4}$$

the wave angle of the plume shock wave is

$$\beta_e \approx 14.92 - 1.252M_\infty + 0.125M_j - 0.146p_r + 1.654\rho_r, \tag{5}$$

and the wave angle of the trailing shock wave is

$$\beta_t \approx 18.24 - 1.282M_\infty - 0.047M_j + 0.349p_r - 0.242\rho_r. \tag{6}$$

Equation 4 is a multivariate polynomial regression model developed to approximate the internal shock angle β_i. This empirical model is derived using least squares regression, where coefficients are optimized to minimize the error

between predicted and actual values. It incorporates linear, quadratic, and interaction terms to capture nonlinear relationships and coupling effects among variables. Validation is performed by comparing the model's predictions with simulation or experimental results, ensuring accuracy within the defined range of conditions. Only β_i uses polynomial regression due to the complexity of the internal shock waves dynamic, while β_e and β_t employ linear regression models (see Eqn. 5 & 6), as their relationships are sufficiently described using simple linear terms.

Figure 15a compares the internal shock waves angle β_i predicted by the FUN3D simulations and the empirical model as a function of the jet Mach number M_j. The FUN3D data β_i^{FUN3D} exhibits a non-linear behavior, decreasing between $M_j = 7$ and $M_j = 9$, followed by a steady increase for higher M_j. This trend reflects the complex interplay between flow properties and the shock wave angle. The empirical model $\beta_i^{\text{Empirical}}$ captures the overall trend but consistently under-predicts β_i, especially at lower M_j values. The RMSE is calculated as RMSE = 0.3382 degrees, corresponding to 3.65% of the average β_i^{FUN3D}, indicating strong agreement between the model and simulation data.

The sensitivity analysis highlights that the dominant contributors to β_i are the terms involving M_j, M_j^2, and their interactions with p_r and ρ_r. These terms account for most of the variations in β_i, emphasizing the importance of jet dynamics in determining the shock wave angle. Secondary contributors such as M_∞, p_r^2, and interaction terms like $p_r\rho_r$ play a more subtle role, providing fine-tuning to the model's predictions. Including quadratic and interaction terms enables the model to capture non-linear effects, such as transitions between weak and strong shock wave regimes. However, the consistent under-prediction of β_i for $M_j = 7$ to $M_j = 9$ suggests potential areas for refinement in the empirical model. Despite these minor discrepancies, the model demonstrates strong accuracy and reliability, effectively capturing the underlying physics of internal shock wave behavior with minimal error.

Figure 15b compares β_e from the FUN3D numerical simulation data and the empirical model from Eqn. 5. The FUN3D data exhibits a nonlinear trend, decreasing shock wave angle for $M_j = 7$ to $M_j = 9$ and increasing for higher M_j. The empirical model captures this overall trend but under-predicts β_e, particularly at lower and higher Mach numbers. The RMSE between the FUN3D data and the empirical model is RMSE = 0.3382 degrees, approximating to 3.65% of the average β_e. This demonstrates that the empirical model closely follows the numerical solution with minor deviations.

The plot in Fig. 15c for β_t shows that the FUN3D data remains stable at lower Mach numbers, peaks around $M_j = 9$, and stabilizes for higher Mach numbers. The empirical model captures the declining trend of β_t with increasing M_j but under-predicts the values at $M_j = 7$ and $M_j = 8$. The RMSE for β_t is RMSE = 0.2326 degrees, corresponding to 2.02% of the average β_t.

The sensitivity analysis reveals the dominant contributors to β_e and β_t. For β_e, the most significant term is the constant, followed by the influence of ρ_r, which shows a positive correlation, and M_∞, which has a negative impact. The contributions from M_j and p_r are relatively smaller but provide finer adjustments. For β_t, the constant term is again dominant, followed by the effect of M_∞, significantly reducing β_t. The terms p_r and M_j have smaller contributions, with ρ_r providing the least influence. These sensitivities highlight that β_t is more sensitive to M_∞ and p_r, while β_e is strongly influenced by ρ_r and M_∞.

H. Discussion of Schlieren Contours and Overpressure Dynamics

The schlieren contour in Fig. 10 highlights the internal shock wave structure within the exhaust plume. Alternating compression and expansion waves are clearly visible as discrete shock cells characterized by high-gradient regions in the flow-field. The darker streaks in the contour correspond to the shock waves, marking regions of significant pressure and density variations. These features closely resemble those observed in Fig. 2.a, where schlieren imaging from the NASA GRC supersonic tunnel at NPR = 14 captures similar shock cell patterns. In Fig. 2.a, the Rayleigh-Pitot tube in the near-field region captures downstream interactions of the plume's shock waves. The experimental schlieren image reveals the shock waves as white streaks of light highlighting the interaction between the internal shocks and the plume's boundary layer.

Additionally, regions of expansion between these compression waves contribute to the formation of discrete shock cells, producing the characteristic "diamond-shaped" patterns often observed in supersonic jets. However, the internal shock structures prominently interact at three distinct points downstream beyond which no further shock cell structures are observed for both numerical simulation and the experiment. This absence of downstream shock formation indicates that the coherent diamond-shaped shock-expansion patterns cease beyond these interaction points. The lack of shock formation downstream is attributed to the static pressure match behind the terminating shock waves.

The overpressure profile in Fig. 11 further supports these observations, showing peaks and valleys in $\Delta p/p_\infty$ along the plume's centerline that correspond to the compression and expansion waves visualized in the schlieren images.

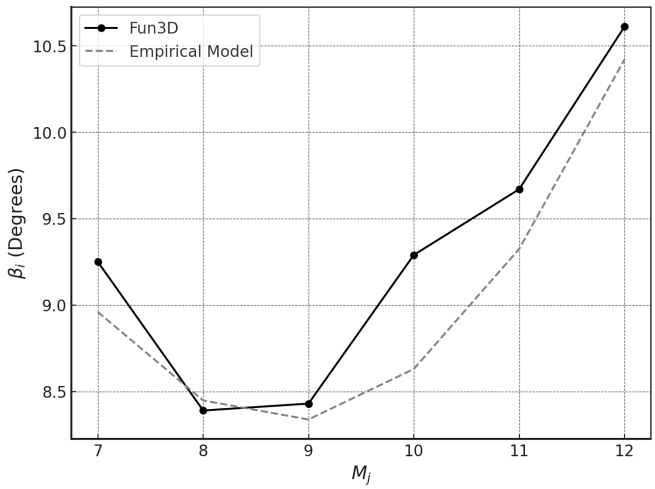

(a) Internal Shock Waves Angle

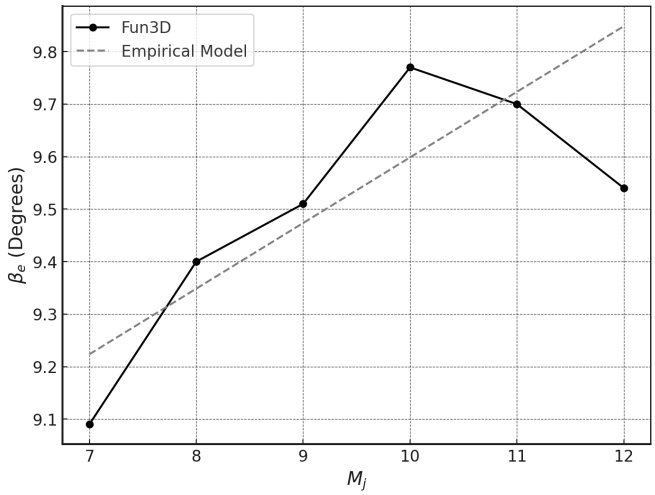

(b) Plume Shock Waves Angle

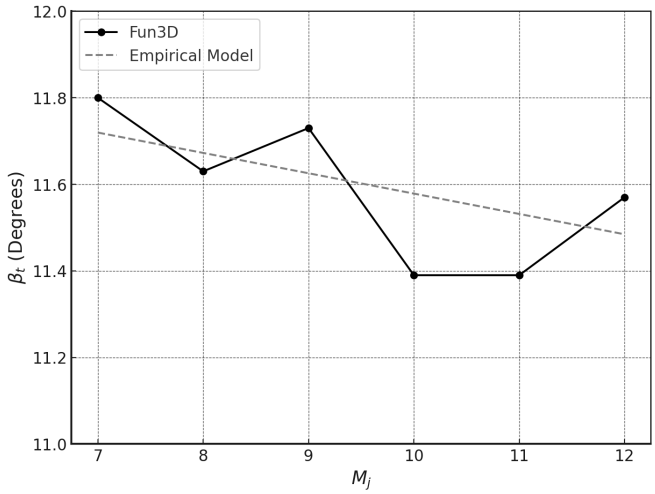

(c) Trailing Shock Waves Angle

Fig. 15 Shock wave angles obtained using FUN3D and the empirical model at $M_\infty = 6$, SPR = 7.00, and STR = 6.91. The plots compare the angles for (a) internal, (b) plume, and (c) trailing shock waves.

While the trends in the overpressure plot are similar to those in Fig. 2b, with a prominent pressure peak near $xD^{-1} \approx 4$ and a secondary peak around $xD^{-1} \approx 6$, the magnitude and shape of the profile differ due to variations in the operating conditions. Specifically, differences in M_j, SPR, and STR affect the intensity and spacing of the shock waves, leading to distinct pressure gradients in Fig. 11 compared to Fig. 2b.

Both simulations effectively capture the plume shock waves, including the trailing shock and its associated expansion wave, which contribute to the normalization of pressure downstream. This normalization highlights how the jet plume transitions from a highly structured flow-field dominated by shocks to a more uniform pressure distribution further downstream. Additionally, the strength and location of the plume shock waves, along with the overpressure amplitude, are strongly governed by the values of SPR and M_j. These parameters not only dictate the intensity of the shocks but also determine the spacing between compression and expansion waves, thereby controlling the overall plume behavior.

IV. Conclusions

This study investigates the dynamics of hypersonic jet exhaust flow-fields focusing on the prediction of internal, trailing, and plume shock waves. High-fidelity CFD simulations using the NASA FUN3D solver capture detailed flow features including shock wave structures, expansion waves, and density gradients under off-design conditions. These simulations provide a comprehensive dataset to validate empirical models and establish a framework for analyzing jet exhaust behavior in hypersonic regimes.

The results reveal the relationships between M_j, SPR, STR, and M_∞, demonstrating how these parameters govern shock wave location, strength, and flow interactions. Internal and plume shock waves are identified with precise spatial and angular characteristics, showing sensitivity to variations in jet exit conditions such as M_j, SPR, STR, and freestream parameters M_∞. Plume shock wave locations are strongly influenced by M_j and SPR, with higher values pushing shock waves further downstream and amplifying their strength. Internal shock wave locations and angles are significantly affected by the interactions of M_j with ρ_r, reflecting the density-driven dynamics of compressible jets. STR dampens downstream pressure oscillations by promoting thermal diffusion while higher SPR intensifies near-field compression waves increasing shock wave prominence.

Empirical models developed in this study predict the origins and angles of internal and plume shock waves with high accuracy, achieving RMSE as low as 3.6% for plume shock wave origins and 3.65% for internal shock wave angles. These models incorporate nonlinear interactions through power-law and cross-interaction terms, offering reliable shock wave property estimates without requiring costly computational simulations. Sensitivity analyses show that plume shock wave origins are primarily governed by M_j and SPR, while internal shock wave origins depend heavily on ρ_r and its interaction with M_j. Shock wave angles β_e, β_i, and β_t are determined by combinations of M_∞, M_j, and SPR, enabling accurate descriptions across a wide range of conditions.

These empirical models provide future researchers with efficient tools to predict shock wave dynamics for hypersonic jet exhaust flows, eliminating the need for resource-intensive simulations. Researchers can use the models to estimate shock wave locations and angles for various operating conditions, making them valuable for preliminary design studies and parametric analyses. The models also serve as a foundation for integrating shock wave dynamics into larger frameworks such as sonic boom propagation models or hypersonic vehicle optimization tools. By bypassing expensive CFD simulations, these models significantly reduce computational costs and accelerate the development of hypersonic systems.

Key findings include the impact of M_j on shock wave strength and plume shock wave locations, with higher M_j amplifying shock wave strength and delaying plume shock wave formation downstream. STR stabilizes downstream flow by promoting thermal diffusion while higher SPR shifts plume shock waves further downstream by intensifying compression waves. Shear layer interactions play a critical role in shaping shock wave angles and locations, with plume shock waves re-compressing the flow after trailing shock waves. Internal shock waves cause localized increases in density and temperature emphasizing their role in compressible jet dynamics.

The modified HLLE++ scheme combined with adjoint-based mesh refinement enables accurate resolution of complex shock wave structures even in extreme hypersonic conditions. These simulations and empirical models establish a foundation for improving predictive capabilities in jet exhaust flows, advancing hypersonic flight system designs, and enhancing sonic boom prediction.

Future work could explore extending the empirical models to account for nozzle geometry variations such as rectangular nozzles and incorporate real gas effects, turbulence, and viscous dissipation. Further validation against experimental data is recommended to improve model accuracy and applicability. Additional studies on higher-order shock wave interactions and multi-phase flow effects would provide deeper insights into plume dynamics. These efforts

could support the design of low-boom high-speed vehicles and advance the understanding of jet exhaust behavior in hypersonic regimes.

Acknowledgments

Research was sponsored by the Defense Advanced Research Project Agency (DARPA) and the Army Research Office and was accomplished under Grant Number W911NF-21-1-0342. The views and conclusions contained in this document are those of the authors and should not be interpreted as representing the official policies, either expressed or implied, of the Army Research Office or the U.S. Government. The U.S. Government is authorized to reproduce and distribute reprints for Government purposes notwithstanding any copyright notation herein.

References

[1] Loubeau, A., and Coulouvrat, F., "Effects of Meteorological Variability on Sonic Boom Propagation from Hypersonic Aircraft," *AIAA Journal*, Vol. 47, No. 11, 2009, p. 2632–2641. doi:10.2514/1.41337.

[2] Plotkin, K., "Review of Sonic Boom Theory," *12th Aeroacoustic Conference*, American Institute of Aeronautics and Astronautics, San Antonio, TX, U.S.A., 1989, AIAA Paper 1989-1105. doi:10.2514/6.1989-1105.

[3] Rathsam, J., Coen, P., Loubeau, A., and Ozoroski, L., "Scope and Goals of NASA's Quesst Community Test Campaign with the X-59 Aircraft," *14th ICBEN Congress on Noise as a Public Health Problem*, NASA, International Commission on Biological Effects of Noise (ICBEN), Belgrade, Republic of Serbia, 2023.

[4] King, C. B., Skowron, S. M., and Miller, S. A. E., "Fully Parabolized Hypersonic Sonic Boom Prediction with Real Gas and Viscous Effects," *AIAA Journal*, Vol. 62, No. 5, 2024, p. 1683–1700. doi:10.2514/1.j063425.

[5] Castner, R., "Exhaust Nozzle Plume Effects on Sonic Boom," *Journal of Aircraft*, Vol. 49, No. 2, 2012, pp. 415–422. doi:10.2514/1.C031305.

[6] Capone, F. J., and Putnam, L. E., "Experimental determination of equivalent solid bodies to represent jets exhausting into a Mach 2.20 external stream," Tech. Rep. NASA-TN-D-5163, NASA Lewis Research Center, 1969.

[7] Castner, R., Elmiligui, A., and Cliff, S., "Exhaust Nozzle Plume and Shock Wave Interaction," *51st AIAA Aerospace Sciences Meeting including the New Horizons Forum and Aerospace Exposition*, American Institute of Aeronautics and Astronautics, 2013, AIAA Paper 2013-12. doi:10.2514/6.2013-12.

[8] Lee-Rausch, E. M., Rumsey, C. L., and Park, M. A., "Grid-Adapted FUN3D Computations for the Second High-Lift Prediction Workshop," *Journal of Aircraft*, Vol. 52, No. 4, 2015, pp. 1098–1111. doi:10.2514/1.C033192.

[9] Venkatakrishnan, V., "Convergence to Steady State Solutions of the Euler Equations on Unstructured Grids with Limiters," *Journal of Computational Physics*, Vol. 118, No. 1, 1995, pp. 120–130. doi:10.1006/jcph.1995.1084.

[10] Nielsen, E. J., "Aerodynamic Design Sensitivities on an Unstructured Mesh Using the Navier–Stokes Equations and a Discrete Adjoint Formulation," Ph.D. Dissertation, Virginia Polytechnic Institute and State University, Blacksburg, VA, 1998.

[11] Diskin, B., Thomas, J. L., Nielsen, E. J., Nishikawa, H., and White, J. A., "Comparison of Node-Centered and Cell-Centered Unstructured Finite-Volume Discretizations: Viscous Fluxes," *AIAA Journal*, Vol. 48, No. 7, 2010, pp. 1326–1338. doi:10.2514/1.44940.

[12] Castner, R., Zaman, K., Fagan, A., and Heath, C., "Wedge Shock and Nozzle Exhaust Plume Interaction in a Supersonic Jet Flow," *Journal of Aircraft*, Vol. 54, No. 1, 2017, pp. 125–134. doi:10.2514/1.C033623.

[13] Biedron, R. T., Carlson, J.-R., Derlaga, J. M., Gnoffo, P. A., Hammond, D. P., Jacobson, K. E., Jones, W. T., Kleb, B., Lee-Rausch, E. M., Nielsen, E. J., Park, M. A., Rumsey, C. L., Thomas, J. L., Thompson, K. B., Walden, A. C., Wang, L., and Wood, W. A., "FUN3D Manual: 13.7," Tech. Rep. NASA/TM–20205010139, NASA Langley Research Center, Hampton, Virginia, November 2020. (Corrected Copy).

[14] Rallabhandi, S., "Sonic Boom Adjoint Methodology and its Applications," *29th AIAA Applied Aerodynamics Conference*, American Institute of Aeronautics and Astronautics, HI, United States, 2011, AIAA Paper 2011-3497. doi:10.2514/6.2011-3497.

[15] Michal, T., and Krakos, J., "Anisotropic Mesh Adaptation Through Edge Primitive Operations," *50th AIAA Aerospace Sciences Meeting including the New Horizons Forum and Aerospace Exposition*, American Institute of Aeronautics and Astronautics, Nashville, TN, United States, 2012, AIAA Paper 2012-159. doi:10.2514/6.2012-159.

[16] Park, M. A., "Anisotropic Output-Based Adaptation with Tetrahedral Cut Cells for Compressible Flows," Ph.D. Dissertation, Massachusetts Institute of Technology, Cambridge, MA, United States, September 2008.

[17] Venditti, D. A., "Grid Adaptation for Functional Outputs of Compressible Flow Simulations," Ph.D. Dissertation, Massachusetts Institute of Technology, Cambridge, MA, United States, June 2002.

[18] Cui, P., Zhou, G., Zhang, Y., Jia, H., Wu, X., Ma, M., Li, H., and Chen, B., "Improved Delayed Detached-Eddy Investigations on the Flow Control of the Leading-Edge Flat Spoiler of the Cavity in the Low-Aspect-Ratio Aircraft," *Aerospace*, Vol. 9, No. 9, 2022, p. 526. doi:10.3390/aerospace9090526.

[19] Anderson, W. K., Biedron, R. T., Carlson, J.-R., Derlaga, J. M., Diskin, B., Jr., C. T. D., Gnoffo, P. A., Hammond, D. P., Jacobson, K. E., Jones, W. T., Kleb, B., Lee-Rausch, E. M., Liu, Y., Nastac, G. C., Nielsen, E. J., Padway, E., Park, M. A., Rumsey, C. L., Thomas, J. L., Thompson, K. B., Walden, A. C., Wang, L., Wood, S. L., Wood, W. A., and Zhang, X., "FUN3D Manual: 14.0.2," Tech. Rep. NASA/TM-20230004211, NASA Langley Research Center, Hampton, Virginia, United States, 2023.

[20] Nastac, G., Tramel, R., and Nielsen, E., "Improved Heat Transfer Prediction for High-Speed Flows over Blunt Bodies using Adaptive Mixed-Element Unstructured Grids," *AIAA SciTech 2022 Forum*, American Institute of Aeronautics and Astronautics, San Diego, CA, U.S.A., 2022. doi:10.2514/6.2022-1086.

[21] Yang, H. Q., and Harris, R. E., "Development of Vertex-Centered High-order Schemes and Implementation in FUN3D," *AIAA Journal*, Vol. 54, No. 12, 2016, pp. 3742–3760. doi:10.2514/1.J054561.

[22] van Albada, G. D., van Leer, B., and Roberts, W. W., "A Comparative Study of Computational Methods in Cosmic Gas Dynamics," *Astronomy and Astrophysics*, Vol. 108, 1982, pp. 76–84. Accessed: May 22, 2024.

[23] Kermani, M. J., Gerber, A. G., and Stockie, J. M., "Thermodynamically Based Moisture Prediction Using Roe's Scheme," *4th Conference of Iranian Aerospace Society*, Vol. 3, Amir Kabir University of Technology, Tehran, Iran, 2003, pp. 1–10.